# UCLA
## UCLA Electronic Theses and Dissertations

**Title**

Achieving a Biomechanically Relevant Model of the Scaphoid with 3D Printing Techniques

**Permalink**

https://escholarship.org/uc/item/8r1812qh

**Author**

Hookasian, Erika

**Publication Date**

2024

Peer reviewed|Thesis/dissertation

UNIVERSITY OF CALIFORNIA

Los Angeles

Achieving a Biomechanically Relevant Model of the Scaphoid

with 3D Printing Techniques

A thesis submitted in partial satisfaction of the requirements for the degree

Master of Science in Bioengineering

by

Erika Hookasian

2024

ABSTRACT OF THE THESIS


Achieving a Biomechanically Relevant Model of the Scaphoid

with 3D Printing Techniques


by


Erika Hookasian


Master of Science in Bioengineering

University of California, Los Angeles 2024

Professor Sophia Nicole Sangiorgio, Co-Chair

Professor Andrea M. Kasko, Co-Chair

Preclinical evaluation of orthopaedic implants typically employs a comprehensive approach, including animal models, cadaver studies, computational analyses, and composite surrogates. Cadaveric models have been integral to the in vitro biomechanical testing of orthopaedic implants and surgical techniques, yet natural anatomic variations in size, shape, and bone quality often overshadow differences due to the experimental variables in these studies. Over the past three decades, commercially available composite bones have been widely accepted as surrogates for biomechanical testing. These epoxy and polyurethane-based models are typically made by injection molding and have been validated by numerous labs for long bone models. However, these models have not been validated or widely adopted for small bones. One explanation may

be that they may not have the resolution needed for biomechanical models of small bones, such as the carpal bones of the upper extremities, which have unique size and mechanical properties. Therefore, the present study investigated the use of additive manufacturing to develop a model of the most commonly fractured small carpal bone, the scaphoid, for the purposes of biomechanical testing.

Scaphoid morphology and bone density were measured through computed tomography to replicate in the model. The strength of three commonly used additive manufacturing materials, polylactic acid, polycarbonate, and resin, was measured at different infill densities. A nonhomogeneous, anisotropic scaphoid model was additively manufactured with polycarbonate, which may be the material most representative of the scaphoid bone from those tested. This model may enable better testing and characterization of surgical implants for the scaphoid.

The thesis of Erika Hookasian is approved.

Jun Chen

Jennifer Lynn Wilson

Andrea M. Kasko, Committee Co-Chair

Sophia Nicole Sangiorgio, Committee Co-Chair

University of California, Los Angeles

2024

# ACKNOWLEDGEMENTS

TABLE OF CONTENTS

**Chapter 1: INTRODUCTION**

**1.1 History of Composite Long Bones**

Composite bone models were developed to enhance in vitro biomechanical testing due to the inherent limitations of cadaveric models. Cadaveric models have been integral to the in vitro biomechanical testing of orthopaedic implants and surgical techniques.[1-4] However, acquiring specimens of similar size, shape, and bone quality has often complicated the implications of cadaveric studies. To circumvent this issue, synthetic bone models replicating the structural properties of cortical and cancellous bone were developed for the femur.[5,6] Since then, decades of refinement and validation of femur and knee models have provided valuable insight into implant development and revision.[5-11] Additionally, composite models have enhanced long-term fixation methods through cycling loading tests.[12-14] These models have allowed for small to no inter-specimen differences for biomechanical testing, allowing even subtle differences in implant design to be characterized.[5-14] Currently, multiple companies manufacture composite bones commercially available for purchase and testing.[15]

Conventionally manufactured bone models have focused on replicating bone by using a foam-like interior to model the inner trabecular bone and a solid, epoxy-based outer shell to model the cortical shell of bone.[15] Rigid polyurethane foam is currently a popular choice of material for cancellous bone, as it can be manufactured in various porosities, replicating various levels of bone density.[15,16] Composite models of polyurethane foam are injection molded with fiber-reinforced epoxy to achieve the cancellous and cortical properties of bone, as seen in Figure 1.[15]

While the validation for composite lower extremity long bones has been achieved, the validation of upper extremity small bone models made with the conventional manufacturing processes has been lacking as it's unknown if these biomechanical properties are sufficient representations of small bones.[15]
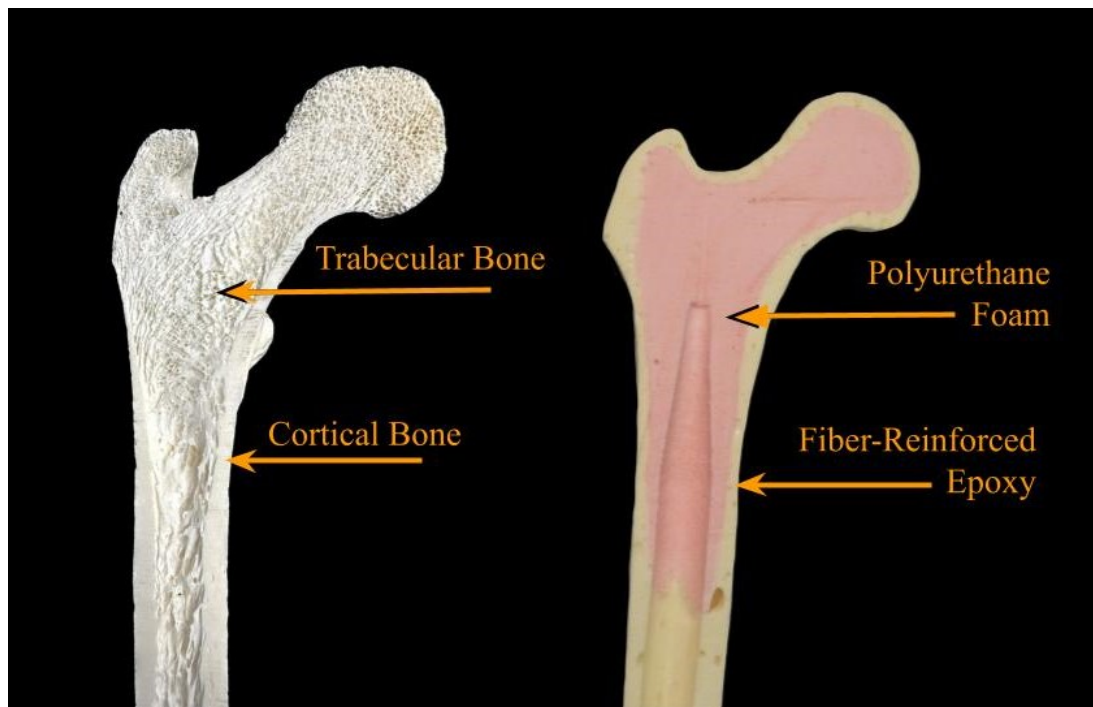


Figure 1: Cortical and trabecular areas of real bone (left) compared to modeled cortical and trabecular regions in synthetically manufactured bone (right).

## 1.2 Small Bone Biomechanical Testing in Cadavers

One of the most commonly fractured small carpal bones of the hand is the scaphoid, which is, therefore, of most interest for biomechanical testing (Figure 2).[17,18] Several studies have attempted to compare methods of fracture fixation using cadaveric models.[18,19] Unfortunately, similar to the problems with cadaveric studies of long bones, the differences in bone quality and

inter-specimen variability of the scaphoid have limited testing with cadavers, especially with small sample sizes.[18-23] Further, due to pronounced differences in hand dominance, paired analysis using left and right hands as controls often differ widely.[21-23]
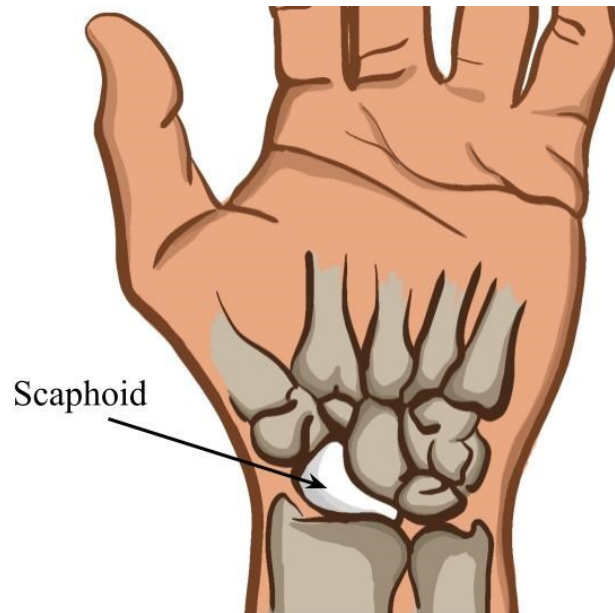


Figure 2: Anatomical location of the scaphoid in the hand.

Differences in scaphoid size and length between genders were suggested in a study by Letta et al., with men having, on average, a 40% larger scaphoid volume, a 20% larger surface area, and a 10% larger length than women.[22] Similarly, another study quantified contralateral differences in carpal bones with computer-based algorithms.[23] Ceri et al. also found significant contralateral differences in 200 cadaveric scaphoids at the circumference of the waist, base of the tubercle, width of the main sulcus, and the secondary height of the tubercle.[21]

Furthermore, the variability of scaphoid bone density has been vastly documented, both as a function of age and throughout the scaphoid itself.[20-24.] Swanstrom et al. observed a decrease in

bone density from the outside surface of the scaphoid toward the inside, and Morimoto et al. documented significant decreases in bone mineral density as a function of age.[20, 25] As a result, a few studies have attempted to use commercially available models for reproducible, consistent methods of evaluating fracture fixation of the scaphoid without the variability that is observed in cadaver models.

**1.3 Small Bone Biomechanical Testing in Composite Models**

A few studies have used the same polyurethane foam model validated for long bones to evaluate methods of fracture fixation in small bones.[26,27] For example, one study used polyurethane foam cylinders with and without an additional cortical shell to model a scaphoid and evaluate the pull-out forces of headless compression screws.[27] They observed that the imitation cortico-cancellous models behaved differently than just foam models, suggesting that the resultant behavior of fixation methods can depend on the bone density used in the model.[27] As morphological parameters may explain 49%–68% of the variation in fracture toughness in real bone, these parameters are critical to match in a synthetic model.[33] However, none of the synthetic scaphoid models previously used were able to take the non-homogeneity of the scaphoid bone density into account or validate their models against cadavers. Additionally, the inherent isotropy of the foam may have been an oversimplification of the anisotropic model of the scaphoid bone, resulting in misleading results.

Given the variability in scaphoid morphology in the literature and a lack of validated synthetic models, there may be an opportunity to create a tunable model using additive manufacturing. In

addition to ensuring greater standardization in biomechanical testing, being able to manipulate the scaphoid microarchitecture to achieve personalized models, such as models with osteoarthritis, contralaterally different models, and specific sizes to represent male and female bones, can allow us to better predict the most optimal fixation modality for a given scaphoid anatomy. To create a more representative synthetic bone, additive manufacturing offers an attractive avenue for printing non-homogeneous, anisotropic models.[16]

## 1.4 The Role of Additive Manufacturing Processes in Scaphoid Models

Many advances in material fabrication over the last few decades have facilitated the process of creating a nonhomogeneous, anisotropic model of bone.[8] These bone models are increasingly popular in surgical training, education, pre-surgical planning, and creating patient-specific guides, implants, and prosthetics.[47] A previous study has validated that additive manufacturing techniques can accurately and reproducibly fabricate carpal bony models despite their small size.[28] However, a biomechanical analysis was not done on the models as their use for that study was primarily for surgical planning and training.[28]

Additive manufacturing, or 3D printing, is a process through which computer-aided design (CAD) models are printed by adding materials layer by layer.[28] A standard tessellation language (STL) format of the CAD file is generated to communicate with the slicing software that then prepares the model for 3D printing.[28] One of the most common additive manufacturing methods includes fused-deposition modeling (FDM), which adds thermoplastic filaments layer by layer on a build platform.

Another method of additive manufacturing is Stereolithography (SLA).[28] In this method, a photocurable resin is solidified through photopolymerization via a computer-controlled laser beam. The quality of an SLA print is dependent on the energy of the light from the laser, the curing depth, layer thickness, and the post-curing process, which can introduce many variables across batches if not carefully controlled. SLA printing can print very high-resolution parts as small as 10 μm, while FDM can print up to 40 μm.[28] However, FDM is a simpler and more streamlined process requiring no post-curing.

Both methods were used in the present study to compare the ease of printing an anisotropic structure and the mechanical properties of the different materials that can be printed with the respective methods. This was the first study to biomechanically evaluate a 3D-printed scaphoid to investigate its use in future evaluations of fracture fixation.

**1.5 Biomechanical Requirements of a Synthetic Model of the Scaphoid**

*Microarchitecture*

Microarchitecture of the bone may be essential to replicate for a synthetic scaphoid model due to the bone's small size. In particular, fracture fixation stability has previously been reported to rely heavily on bone quality. [30-33] Ideal fracture fixation requires adequate bone density for bone purchase of screws.[25] Bone mineral content has been reported to be the most important element contributing to bone strength, as risk of fracture is directly proportional to the bone structure.[29-33] Fracture risk increases considerably when the bone mass decreases.[34] A higher bone density contains a larger number of osteons per unit of bone volume, which can obstruct crack

6

propagation once there is a crack formation and limit how far the crack can propagate as it navigates between the many osteons.[33] Accordingly, a synthetic model needs to consider the resolution needed for this microstructure, as even small cracks can be more significant in the small scaphoid model than in the model of a larger long bone. Besides modeling accurate crack propagation at failure, the model needs to display behaviors similar to that of cadaver bone when fixed.

*Material Interactions with Fixation Methods*

Another consideration for a more representative model of the scaphoid is the method in which it interacts with the metals used to fix fractures. One simple and quick method of fixation of hand bone fractures includes the percutaneous drilling of Kirschner wires (K-wires) using a power drill.[35] Successful fixation with these smooth wires requires the drilled hole to be precise and also depends on the secondary changes in the bone caused by the drilling process.[35] A previous study has suggested that during drilling, the friction that exists between the bone and the metal K-wire may create conditions in which the adjacent bone to the K-wire can cause osteonecrosis and loss of stability.[35,36] Additionally, they mention that the drilling debris produced when using K-wires may not be cleared and can impact biomechanics and stability. [36] Material considerations for synthetic materials need to withstand melting or deforming dissimilarly to the real bone when experiencing these high temperatures during drilling ( > 70 degrees Celsius).[35] Therefore, to test the implant stability of small carpal bones in synthetic models, the microarchitecture and drilling ability should be as close as possible to what is observed in the cadaver models.

**1.6 Material Selection**

To investigate biomechanically relevant materials that could replicate bone strength, while also keeping in mind the need to replicate the scaphoid's microarchitecture and model how it would interact with known fixation methods, three materials were considered: Polylactic Acid (PLA), Polycarbonate (PC), and White Resin.

*Polylactic Acid*

Polylactic Acid (PLA) has been commonly used as a 3D-printed material for bone and has been shown to perform mechanically better in ultimate force and stiffness when compared to existing polyurethane-based models.[37] It has been shown to exhibit the same trend of increasing force with increasing density as seen in real bone, but it still may not provide the same stiffness or strength as strong bones like the femur.[37] This is less of a disadvantage for a small bone, such as the scaphoid, which sees considerably less force and loading cycles than a femur.[18,2] A disadvantage to using PLA is that a PLA model may melt locally while being machined or drilled.[16,35] This is an important and potentially problematic feature, as K-wires and screws that are inserted in a scaphoid model would require local frictional forces to stay in place. Creating a model with PLA that may melt locally and adhere to these implants would change the frictional forces at play and, therefore, may not be representative of clinical conditions.

*Polycarbonate*

Polycarbonate (PC) has been suggested for use as an adequate surrogate for human cadaver bone.[38,39] Specifically, one study looked at four different materials, one of which was

polycarbonate, to use for skull base surgery simulation and found that it was the best material of the four.[38] Forces needed to break polycarbonate structures were 1.6-2.5 times higher than bone, and energy spent drilling through polycarbonate was 1.6 times higher than bone.[38] The polycarbonate proved to be a better material to represent bone than the resin, polyamide, and calcium sulfate hemihydrate materials.[38]

Additionally, another study compared polycarbonate, acrylonitrile butadiene styrene, photopolymerizable polymer, and two types of photo-cross-linkable acrylic resin, white and blue, to print a temporal bone model that would most accurately recreate a cortical mastoidectomy.[39] They found that the polycarbonate replicated the surgical drilling and printing accuracy required for the surgical training models. [39]

*White Resin*

White resin was one of the other materials tested in the 3D-printed temporal bone study.[39] In the previous study on replicating a surgical model of a temporal bone, it was found to have superior functional aspects of drilling, including texture, odor, powder generation, and pitch change.[39] Furthermore, it had high accuracy during printing and replicated the accuracy of surgical drilling and printing just as well as polycarbonate. [39] However, the biomechanical strength was not explored.

## 1.7 Replicating Anisotropy

To replicate the anisotropy observed in bone, previous studies looking to replicate the structure of bone have used the gyroid structure, which is commonplace in additive manufacturing and can be used to replicate bone porosity.[16,40-41] For example, in our previous study, we compared the strengths and stiffnesses of common infill patterns at different densities used in printing PLA material and found the gyroid structure to be ideal for matching a vertebral structure of the cervical spine due to its strength at different porosities.[40] The failure method of the gyroid structure was also most similar to that of cadaveric bone.[40] Similarly, another group found the gyroid structure presented better behavior even when compared at 100% density to the 100% linear infill models in high-speed compression tests.[41] This suggested that the orientation of the filament had a large impact on the results.[41] They described the highly intricate and porous gyroid structure as unique to additive manufacturing, such that it cannot be achieved easily with traditional manufacturing.[41] Therefore, the gyroid structure was used as the default for all materials in the present study. However, further research is needed in this area as there may be better patterns that can replicate the anisotropic nature of the bone in the future.

**Chapter 2: METHODS**

*2. 1 Morphological Measurements*

Cadaver specimens were acquired through a licensed willed body program. Nine pairs of fresh-frozen cadaveric arms were used (n =18). After the scaphoids were dissected from each arm and freed from attached soft tissue, radiographs were taken of each bone to ensure there were no prior surgeries, fractures, or abnormalities. Morphological measurements, such as the long axis length, as well as the width and thickness of the proximal, waist and distal areas, were recorded. Commercially available scaphoid models are made to be reliably uniform, so similar measurements were taken for one commercially available left synthetic scaphoid to compare (Sawbones Inc., WA, USA).

The Coefficient of Variation (CV) was calculated with the formula below to understand the variation of the specimens within the context of the scaphoid's small average size:

$$CV = \frac{\sigma}{\mu}$$

*Where $\sigma$ = the standard deviation of the measurement and $\mu$ = the average value*

*2. 2 CT Scanned Scaphoids*

Seven scaphoids were scanned with a CT scanner and XCT analysis (Stratec Medizintechnik GmbH, Pforzheim, Germany). Bone density was measured for the cortical and trabecular regions of the bone. Figure 3 shows the 1 mm scaphoid slices that were analyzed. The cortical region

was isolated from the trabecular for all slices and was analyzed separately to quantify the bone mineral density.
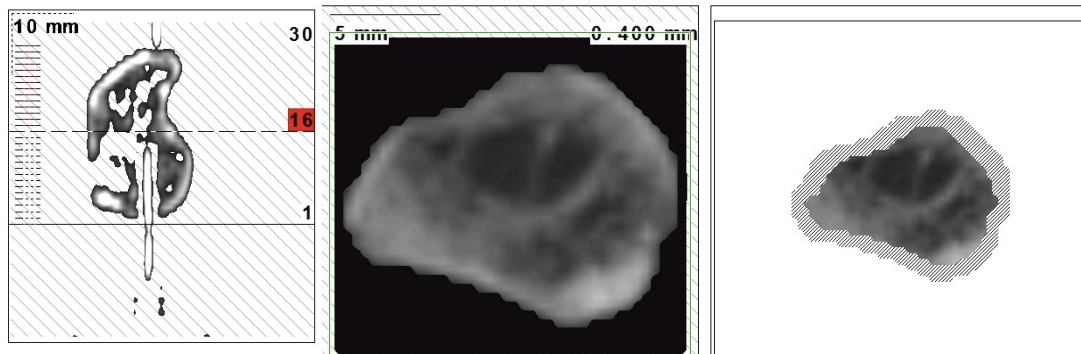


Figure 3: Each scaphoid was sliced with 28-32 CT slices of 1 mm resolution, and each slice was analyzed based on density in the inner trabecular region and the peripheral ring of cortical bone.

As the scaphoid is a small bone, 3D printed structural integrity is increased when regions of density changes are not too small. Therefore, each scaphoid was subdivided into the cortical and inner trabecular shells for analysis. Within the trabecular region, the CT slices were grouped into 5 evenly spaced (5-6 mm)  subregions: the waist and 2 regions of evenly spaced segments on either side of the waist (4 additional regions). The regions were spaced proximal to the distal portion of the scaphoid as shown in Figure 4. These regions were chosen as consistently as possible despite the morphological differences between each cadaver scaphoid.
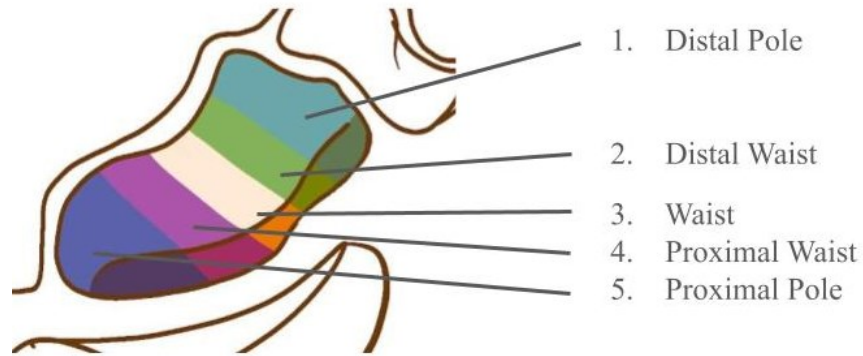
Figure 4: The density of the trabecular region in the seven scaphoid specimens was averaged according to the five areas labeled distal pole (1), distal waist (2), waist (3), proximal waist (4), and proximal pole (5).

CT scan slices were measured and utilized, slice by slice, to reconstruct the scaphoids into 3D printable models. The model was refined to ensure anatomical accuracy by smoothing any jagged edges. Once the model was finalized, it was exported as a stereolithography (STL) file, compatible with 3D printing. Bone density measurements within the scaphoid were used to create different density regions in the model.

## 2. 3 3D Printing Material Analysis

*Literature Review*

The most commonly used 3D printing materials for biomechanical and surgical simulation of bone in current literature were investigated. Polycarbonate, General-Purpose Resin, and Polylactic Acid (PLA) were identified for their strength, hardness, and use in previous studies concerning 3D-printed bone.

*Specimen Preparation*

Specimens were printed according to the ASTM Standard Method of Testing Compressive Properties of Rigid Plastics (D695 – 15) [46] using Ultimaker Cura software (Ultimaker, Zaltbommel, NL) and Formlabs Preform Software (Formlabs, Somerville, MA) to measure compressive strength.



Figure 5: Resin, PC, and PLA specimens at different print densities of the gyroid infill pattern.

As per the ASTM Standard, rectangular specimens of 12.7 x 12.7 x 25.4 mm were printed on an Ultimaker S5 Pro printer using PC and PLA materials with different built-in infill densities. The gyroid lattice structure was previously identified as a good candidate for bone (UltiMaker, Zaltbommel, NL).

Similarly, the resin models were printed using a Formlabs Form 2 printer (Formlabs, Somerville, MA). However, no built-in gyroid model exists in the slicing software as it does for the Ultimaker software. Instead, the prints of different infill densities were first prepared in nTopology (nTopology, New York, NY) with a gyroid setting. To ensure structural infill matching between the two programs, a cross-sectional pattern of the Ultimaker gyroid models at different percentages was used to calculate the number of wavelengths of material used within that cross-section and the number of pores present. These calculations were then used to specify

in nToplogy the number of wavelengths and pores needed within a cross-sectional area. A match was made as close as possible between the infill densities of prints from Ultimaker Cura and those made in nTopology. The resin prints were then printed, dried in an oven, and cured with ultraviolet (UV) light according to the manufacturer's guidelines to achieve complete material properties.

Following ASTM Standard D695, $n = 5$ specimens were tested with each in-fill density percentage and material sample group. In-fill density refers to the percentage of printed material to space utilized within a given structure. While 100% infill density means the entire structure has printed material, the pattern of that material can change the material properties of that structure, hence only the use of a gyroid pattern. Upon completion of successful prints, every combination of variables was tested in compression until failure to assess material strength.

*Compression Testing*

Specimens were tested in compression using a biaxial servo-hydraulic load frame (858 Mini Bionix; MTS Systems, Eden Prairie, MN). Axial load was applied through a ball-and-socket joint to ensure pure compression was applied uniformly across the top surface of the specimens (Figure 3). Following ASTM Standard D695-15, specimens were tested at a rate of $1.3 \pm 0.3$ mm/min, and the load was recorded until they failed. Failure was defined as the formation of any mechanical defect, such as buckling or cracking, during testing.
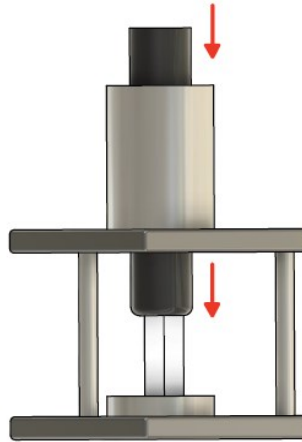
Figure 6: The white block represents the specimens placed in the compression testing setup apparatus. Above this apparatus was a ball and socket joint through which the MTS actuator applied axial load.

*Data Reduction*

A custom MATLAB program (version R2020a; Mathworks, Natick, MA) was developed to calculate the compressive strength and modulus of elasticity. Compressive strength was determined by dividing the compressive yield load by the cross-sectional area. Using displacement and force data from the load frame (858 Mini Bionix; MTS Systems, Eden Prairie, MN), a stress versus strain plot was created for every specimen. The stiffness was calculated from the slope of the linear portion of this curve.

*Strength Relationship*

A best-fit relationship for strength was then calculated for each material. Due to a lack of literature on strength and density relation for upper extremity bones, the widely accepted Carter-Hayes equation was used:

$$S = 68\epsilon^{0.06}\rho^2$$

Where S is the compressive strength (MN/m$^2$) of bone density $\rho$ (g/cm$^3$) tested at a strain rate of $\epsilon$ (sec$^{-1}$).[43]

## 2. 4 Model Creation

A custom 3D model was developed in nTopology using the previously described method of STL creation with separate density regions for each anatomical location. This computer model created the architectural framework for the customizable model. In-fill densities and gyroid structures were assigned to each section to match the previously calculated strength values. Finally, the 3D-printed model was printed to ensure seamless integration of the custom in-fill densities and sufficient print quality.

**Chapter 3: RESULTS**

*3. 1 Scaphoid Morphology Summary*

The dimensions labeled in Figure 7 were measured for all eighteen scaphoid specimens. Table 1 lists all the average measurements for length, distal width, waist width, proximal width, distal thickness, waist thickness, and proximal thickness.
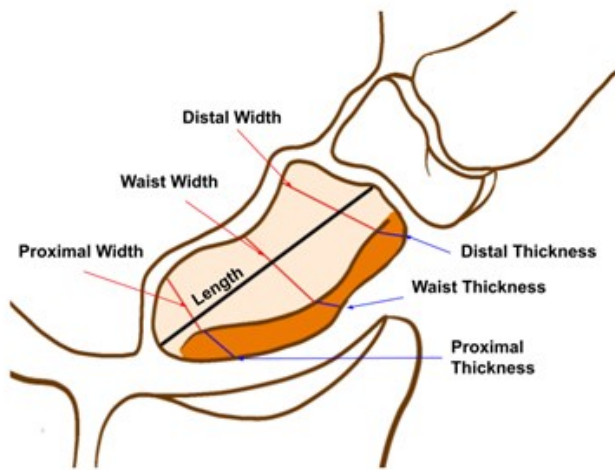


Figure 7: The scaphoid, as positioned in the right hand, is shown above. The proximal to distal center axis was labeled as the length. The width was measured in the coronal plane, and the thickness was measured in the sagittal plane for the distal, waist, and proximal locations,

As seen in Table 1, the waist of the scaphoid had the smallest average value at 10.1 mm, with a range of 7.9 to 12.7 mm, while the length of the scaphoid was, on average, 28.9 mm, with a range of 26.2 mm to 34.9 mm. The measurements for the width of the scaphoid decreased from distal to proximal, with the range of the distal, waist and proximal width measured as 10.2-17 mm, 9.5-15.2 mm, and 7.4-18.7 mm, respectively. The scaphoid thickness across the distal,

waist, and proximal areas were similar, ranging between 9.6-19.5 mm, 9.3-15.6 mm, and 9.3-19.4 mm, respectively.

Table 1: Average Scaphoid Measurements (mm)
Mean (SD)

| Length | | |
|---|---|---|
| 28.9 (2.61) | | |
| Distal Thickness | Waist Thickness | Proximal Thickness |
| 12.8 (2.84) | 12.34 (1.84) | 15.13 (2.69) |
| Distal Width | Waist Width | Proximal Width |
| 13.37 (2.21) | 12.14 (1.82) | 12.98 (3.45) |

Table 2 below shows that the variations amongst measurements ranged from 9-27%.

Table 2: Coefficients of Variation

| Length | | |
|---|---|---|
| 9% | | |
| Distal Thickness | Waist Thickness | Proximal Thickness |
| 22% | 15% | 18% |
| Distal Width | Waist Width | Proximal Width |
| 17% | 15% | 27% |

Similar measurements were taken for the commercially available left synthetic scaphoid (Sawbones Inc., WA, USA). The length was 31.3 mm. The distal, waist, and proximal width values were larger than the cadaver values at 19.6 mm, 15.8 mm, and 12.1 mm, respectively. The distal, mid, and proximal thickness values were much smaller than the cadaver values, at 6.9 mm, 7.8 mm, and 11.3 mm, respectively.

## 3.2 Morphological Variations

One notable variation observed was the difference in male and female scaphoids within our samples. Table 3 lists the average, minimum, and maximum length, distal width, waist width, and proximal width of male and female specimens, along with the standard deviations.

Table 3: The male and female mean, minimum, and maximum values for all lengths, thickness, and width in the distal, waist, and proximal locations.

| | Distal Thickness | | Waist Thickness | | Length | |
|---|---|---|---|---|---|---|
| | M | F | M | F | M | F |
| Mean | 13.9 | 12.2 | 13.6 | 11.0 | 29.4 | 27.3 |
| Std. Deviation | 3.6 | 1.8 | 2.0 | 0.9 | 2.1 | 0.9 |
| Minimum | 10.2 | 10.1 | 10.8 | 9.3 | 26.6 | 26.2 |
| Maximum | 19.4 | 14.7 | 15.8 | 11.9 | 31.7 | 28.4 |

| | Distal Width | | Waist Width | | Proximal Width | |
|---|---|---|---|---|---|---|
| | M | F | M | F | M | F |
| Mean | 14.9 | 12.1 | 12.8 | 10.9 | 12.8 | 10.6 |
| Std. Deviation | 1.6 | 2.0 | 2.3 | 1.2 | 4.6 | 2.2 |
| Minimum | 13.2 | 10.7 | 9.8 | 9.2 | 7.4 | 8.7 |
| Maximum | 17.0 | 16.0 | 15.0 | 12.7 | 18.6 | 15.0 |

The length, distal width, and waist-thickness were all statistically significant ($p < 0.05$), with p-values of 0.043, 0.022, and 0.016, respectively. The waist-width was also different, with a p-value of 0.088, but not statistically significant.
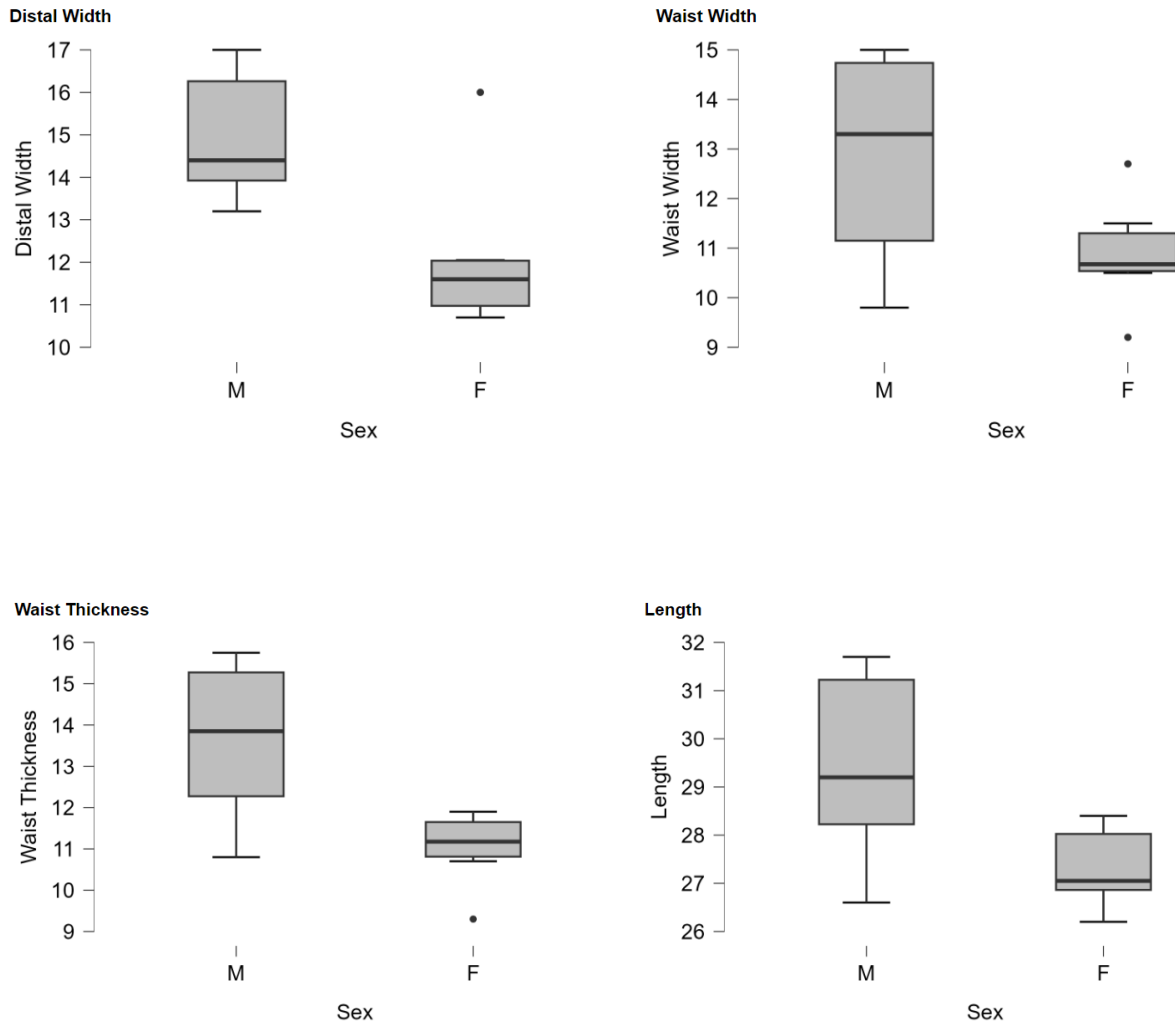
Figure 8: The male and female comparisons of scaphoid distal width (a), waist width (b), waist thickness (c), and length (d).

## 3.3 CT Regions of Interest

Seven scaphoids were CT scanned to obtain slices of bone density measurements. The density of

the trabecular region in the seven scaphoid specimens was averaged according to the previously

defined areas labeled distal pole (1), distal waist (2), waist (3), proximal waist (4), and proximal pole (5).

Table 4: Trabecular density values of the five different regions.

| | Trabecular Density (mg/ccm) | | | | |
| | 1 | 2 | 3 | 4 | 5 |
|---|---|---|---|---|---|
| Mean | 464.9 | 347.5 | 287.4 | 237.9 | 329.5 |
| Std. Deviation | 90.2 | 87.7 | 72.2 | 70.0 | 95.2 |
| Minimum | 338.3 | 240.1 | 215.6 | 146.9 | 222.9 |
| Maximum | 611.7 | 504.6 | 409.0 | 344.1 | 475.0 |

The average density for the distal pole was 464.9 +- 90.2, the distal waist was 347.5 +- 87.7, the waist was 287.4 +- 72.2, the proximal waist was 237.9 +- 70.0, and the proximal pole was 329.5 +- 95.2 mg/ccm. A 5-way ANOVA calculation of the different quadrants yielded a p-value less than 0.001.

To further explore the differences, a post-hoc Tukey test was done. There was a significant difference between the mean bone density of the distal pole and the waist, proximal waist, and proximal end, with p-values of 0.004, 0.001, and 0.037, respectively. The difference between the distal pole and distal waist was also large, with a p-value of 0.091.
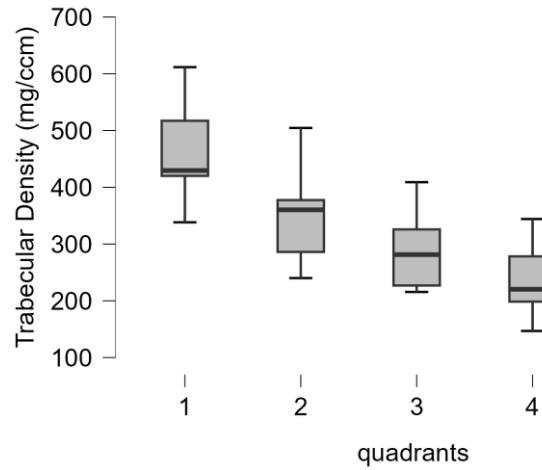
*Trabecular Bone Density*



Figure 9: Average Trabecular Density (mg/ccm) across the five previously defined regions of the

scaphoid specimens.

*Cortical Bone Density*

The density of the cortical bone region in the seven scaphoid specimens was averaged according

to the previously defined areas labeled distal pole (1), distal waist (2), waist (3), proximal waist

(4), and proximal pole (5).

Table 5: Cortical bone density values of the five different regions.

|  | Cortical Density (mg/ccm) | | | | |
|---|---|---|---|---|---|
|  | 1 | 2 | 3 | 4 | 5 |
| Mean | 519.4 | 503.7 | 495.1 | 449.7 | 437.6 |
| Std. Deviation | 96.1 | 87.8 | 79.0 | 73.3 | 68.6 |
| Minimum | 420.4 | 370.3 | 431.0 | 386.0 | 374.4 |
| Maximum | 689.2 | 647.6 | 665.8 | 605.9 | 576.4 |

The average density for the distal pole was 519.4 +- 96.1, the distal waist was 504.7 +- 87.8, the

waist was 495.1 +- 79.0, the proximal waist was 449.7 +- 73.3, and the proximal pole was 437.6

+- 68.6 mg/ccm.  A 5-way ANOVA calculation of the different quadrants yielded a p-value of 0.282.
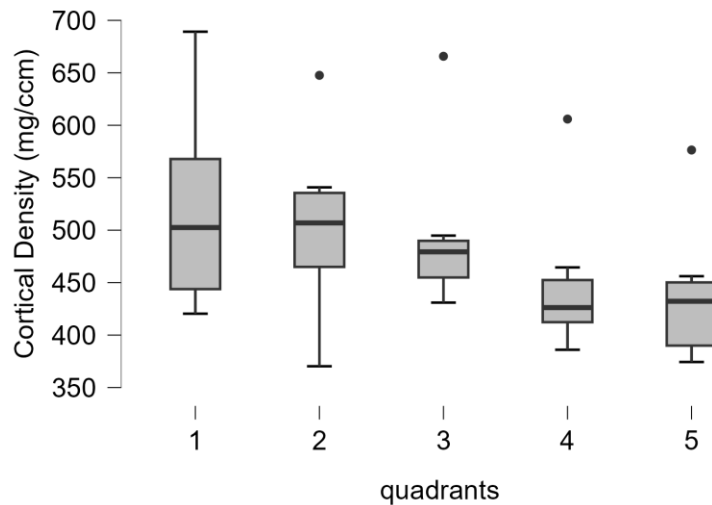


Figure 10: Average Cortical Density (mg/ccm) across the five previously defined regions of the scaphoid specimens.

## 3.4 3D Printing Materials Analysis

*Strength*

A representative model was created for each material from the calculated strengths, relating the in-fill density to the compressive strength. The best-fit line relating the density to strength for the polycarbonate material was exponential, and for the other materials, a quadratic function.
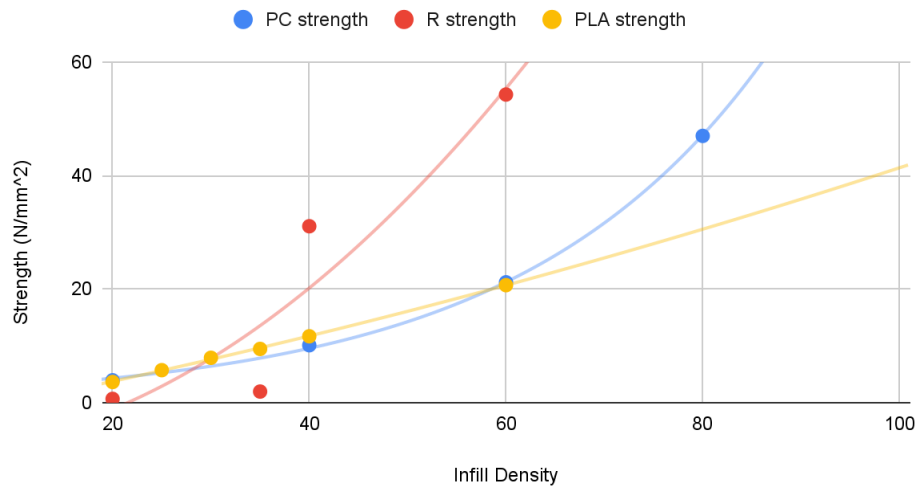
Figure 11: The strength in N/mm$^2$ of polycarbonate (PC), resin (R) , and Polylactic Acid (PLA) were plotted against in-fill density percentage.

Strength (S) Equations for the different materials depending on infill density (x) are provided below:

*Polycarbonate*                 $S = 1.94 * e^{0.04x}$

*Resin*                         $S = 0.02 \, x^2 + 0.03x - 8.7$

*Polylactic Acid (PLA)*         $S = 0.01x^2 - 0.01x - 1.7$

*Stiffness*

The stiffness of the polycarbonate and resin materials was calculated for each specimen from the load versus displacement curves under axial loading. Stress and strain were calculated for all time points and plotted against each other. The stiffness was calculated for each specimen and averaged based on material and in-fill density.
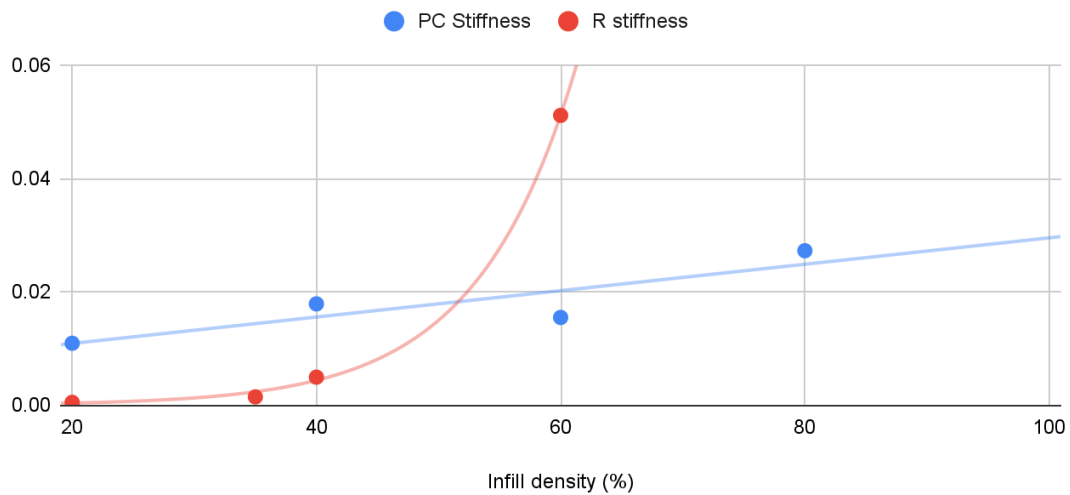
Stiffness of Materials

Figure 12:  The stiffness of the polycarbonate (PC) and resin (R) were evaluated as they were axially

loaded to failure.

The polycarbonate had a linearly increasing stiffness as a function of infill density, and the resin

was best described by an exponential model as described below:

*Polycarbonate*                                        $S = 0.00024 * x + 0.006$

*Resin*                                                        $S = 0.00003 * e^{0.123x}$

### 3.5 Model Creation

A final 3D-printed model based on the previously identified five regions was constructed

following the mathematical relationships and comparison to the calculated strength values.

Polycarbonate material was used in each location based on the compressive strength of the bone.

The STL model was created using the CT scan of a single scaphoid specimen, and the exact

structures and in-fill densities were constructed in each of the five regions with nTopology software. One model was printed using the same melting temperature and print speed to ensure a seamless, non-homogeneous model of the scaphoid (Figure 13).
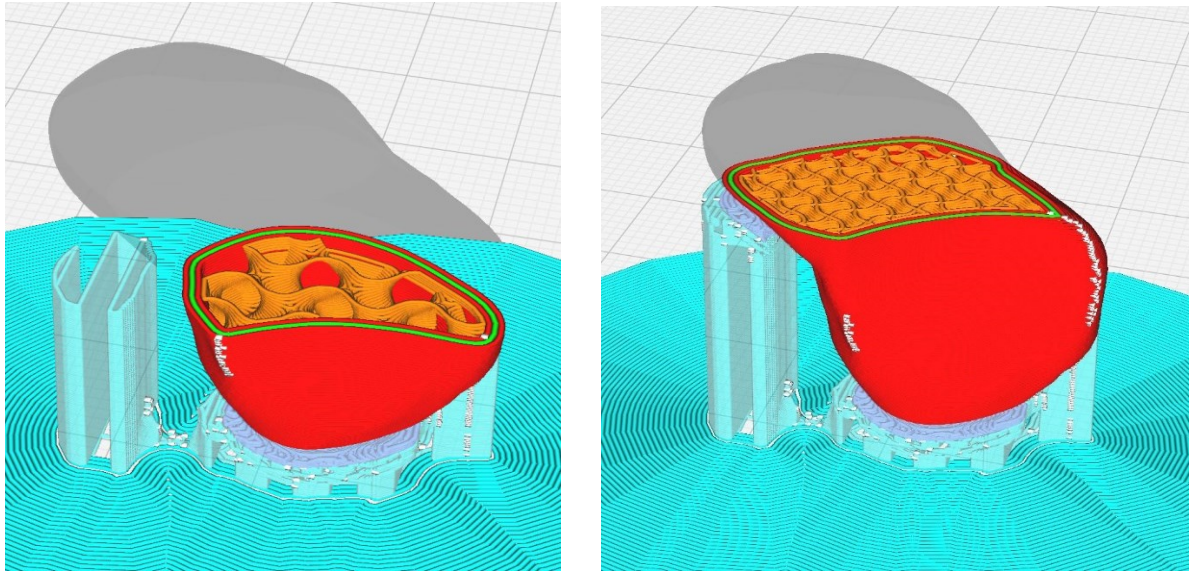


Figure 13: Finalized three-dimensional model showing the infill density of a) in the proximal waist at 16% and b) in the distal waist at 35%.

Table 6: The cortical and trabecular density from CT scans and the respective calculated in-fill density required to match the strength of the real bone.

| | Cortical Bone density (mg/ccm) | Trabecular density (mg/ccm) | Cortical Strength (MPa) | Trabecular Strength (MPa) | Cortical PC Density (%) | Trabecular PC Density (%) |
|---|---|---|---|---|---|---|
| 1- distal pole | 519.4 | 464.9 | 17.7 | 14.2 | 55 | 50 |
| 2- distal waist | 503.7 | 347.5 | 16.7 | 7.9 | 54 | 35 |
| 3- waist | 495.1 | 287.4 | 16.1 | 5.4 | 53 | 26 |
| 4- proximal waist | 449.7 | 237.9 | 13.2 | 3.7 | 48 | 16 |
| 5- proximal pole | 437.7 | 329.5 | 12.6 | 7.1 | 47 | 33 |

# Chapter 4: DISCUSSION

## 4.1 Scaphoid Morphology

The length and width of the scaphoids in the present study were consistent with another study by Mandaleson et al. that measured the dimensions of the scaphoid prior to testing scaphoid fracture fixation methods using a single screw, double screw, or plate (Table 7). [42]

Table 7: The length and width measurements of cadaver scaphoids in a study by Mandaleson et al. and the present study

| Group | Length (mm) Mean (SD) | Width (mm) Mean (SD) | Authors |
|---|---|---|---|
| Single Screw (n =11) | 28.3 (2.5) | 11.7 (1.6) | Mandaleson et al. |
| Double Screw (n = 11) | 28.8 (4.0) | 12.2 (1.7) | Mandaleson et al. |
| Plate (n=8) | 30.0 (3.5) | 12.1 (2.0) | Mandaleson et al. |
| **Intact scaphoids (n = 18)** | **28.9 (2.61)** | **12.2 (1.82)** | **Present Study** |

The variations in scaphoid morphology observed within the different geometrical measurements taken in this study suggest that cadaveric studies may have limitations when assessing implants or surgical techniques for scaphoid fractures, similar to trends in the literature.[19-24] For example, the proximal width had 27% variation within our sample group, with the lowest amount of

variation being the length at 9%. This is still a large amount of variation for such a small bone, as every millimeter of bone may impact the structural integrity of implants used in fracture fixation.[25]

The bone density, scaphoid size, and gender may all be confounding variables inherent to the morphology of scaphoid specimens. Specifically, the present study observed that male scaphoids had a larger length and width across the distal, waist, and proximal locations. As the waist is the most common site of fracture for the scaphoid, the morphological differences for both populations must be accounted for in synthetic models to test the biomechanics of potential implants.[17]

The manufactured scaphoid foam models currently available on the market do not represent the measured dimensions of cadaver scaphoid values in the literature. They may interfere with biomechanical testing due to inadequate bone volume for implant purchase compared to real bone. For example, the synthetic model's distal thickness of 6.9 mm was almost half of the average distal thickness of 12.8 mm we obtained from our cadaver samples. This pattern was followed for the waist and proximal thickness. This is a problem when testing the stability of fixation methods, as a smaller dimension in one plane may create additional instability for a given fixation method. Instead, additive manufacturing allows models to be tuned to the specific need of the study, whether using the averages of these populations, the population as a whole, or even patient-specific values.

*4.2 Bone Density Regions*

Additive manufacturing also allows the tunability of different in-fill density regions, establishing a match between synthetic models and the various anatomical areas of the scaphoid with different bone density and strength values. For simplicity in printing, the scaphoid bones analyzed in this study were split into five regions between the distal and proximal ends. As most scaphoid fixation methods utilize bone friction and bone purchase of the proximal and distal ends, the significant difference that we found between these two regions is critical when testing fixation methods and, consequently, for creating a synthetic model to do so. The cortical shell of the five regions did not have a significant average difference. Still, they followed the same pattern, with the average distal cortical density being higher than the proximal, initially starting to decrease around the waist area.

This finding contrasts a previous study by Swanstrom et al. that found the proximal pole of the scaphoid to have a greater bone density than the distal pole.[25] The difference between the present study and the one by Swanstrom et al. may be due to different definitions of cortical and trabecular regions for the different ends of the scaphoid and the age of the cadaveric specimens used.  A study by Morimoto et al reported significant relations between age and bone mineral density (BMD) in both men's and women's scaphoid bones, with BMD decreasing with age.[20] This finding could explain the difference in findings between the two studies and further emphasizes the need for a synthetic model that can be tuned to different density values depending on age, sex, and other factors.

In the same study by Swanstrom, they analyzed 2 mm shells from the exterior of the scaphoid bone to the interior.[25] They found the exterior shell of the scaphoid had the greatest bone density, with the inner shells significantly decreasing in density.[25] This was reflected in the analysis of this study as well, as the outer "shell" was what we defined as the cortical bone, and the inner portion was trabecular. All five regions that were analyzed as cortical bone (the outer shell) had a higher average bone mineral density compared to the inner trabecular bone. Ahrend et al. summarized the importance of looking at the shape and size of the scaphoid in relation to possible screw or k-wire positioning, finding that the proximal pole of the scaphoid had almost 10% higher mean bone mineral density values than the one near the distal end.[24] They also found that the lowest bone mineral density values were at the waist of the scaphoid.[24]

It is important to note that further studies are required to investigate differences in scaphoid bone density due to age, perhaps by imaging a wide age range of patients. For example, Huntington et al. found no significant differences in bone density and total bone volume between any of the quadrants they defined in the proximal and distal poles of the scaphoids.[48] In contrast, Morimoto et al. found significant relations between age and bone mineral density, with bone mineral density decreasing with age for both men's and women's bones.[20] This may highlight the true nature of the inconsistencies seen between the studies and emphasize the need for a tunable synthetic model that can easily match any desired bone density value.

## 4. 3 Scaphoid Material Analysis

PLA has been used to 3D print various bone structures in the past, such as vertebral models and femurs.[16,37,40,44] This report explored the strength of Polycarbonate (PC) and Resin across various densities as an alternate material to PLA.

In a previous study by Bohl et al., 3D printed vertebral models were modified with different materials, in-fill densities, in-fill patterns, and print orientations to reliably produce a model of bone at a specific bone density.[44] Similarly, Nagl et al. and Metzner et al. were both able to successfully print femoral bones that were comparable to the cadaver and perhaps better than commercially available models due to their specificity in matching bone density and the ability to replicate the anisotropic model of bone.[16,37] However, Metzner et al. noted that the PLA model began to melt locally when being machined during the preparation of the medullary canal.[16] As the purpose of this report was to create a scaphoid model that could be utilized in testing scaphoid fracture fixation methods such as the use of k-wires or screws, which both require drilling, the melting of PLA was concerning. Therefore, two other possible materials were identified from a study by McMillan et al. that achieved 3D-printed temporal bone models as training tools for cortical mastoidectomy, a process that requires drilling.[39] These two materials, FDM-printed polycarbonate and SLA-printed white resin, were identified as relatively cheap and quick alternatives to printing PLA. However, no previous biomechanical studies have been done to quantify strength or stiffness of these materials at various in-fill patterns.

The white resin and the PLA materials were both represented by quadratic functions relating their in-fill density percentage to their strength in $N/mm^2$. However, it was clear that the resin achieved a higher strength value much quicker than the PLA, albeit being less reliable due to the many steps in the printing and curing process as compared to PLA. The polycarbonate was best described by an exponential function, almost matching the behavior of the PLA until an in-fill density of 60%, and then increasing in strength much faster than PLA in densities higher than 60%. Based on strength alone, the white resin and polycarbonate were both viable contenders as an alternate material to PLA for use in the 3D printing of bone.

From a manufacturing perspective, the polycarbonate was much easier to work with as it followed the same process as printing PLA. An Ultimaker S5 was used to print the models seamlessly with polycarbonate. In contrast, the resin had a multistep printing and curing process, potentially resulting in specimens of different strengths despite being printed with the same printer. This can be seen in Figure 11 as the resin is not modeled well by the curve due to large variations in experimental data. The resin at lower densities was also very fragile, breaking on the edges when following the same protocol to place it into the custom compression testing apparatus.

It was interesting to see the difference in stiffness between the two materials, as the polycarbonate had a linear increase in stiffness with an increase in in-fill density, but the resin did not. While the resin appeared to exhibit an exponentially increasing stiffness, more testing is required to validate this as, in reality, the stiffness of specimens under 40% infill density was unpredictable and variable, potentially due to the manufacturing process. It is possible that the

resin did have a higher stiffness at an in-fill density percentage of 60% and above, but the curing of such dense resin materials was not validated in this study. Therefore, based on manufacturing ease and material strength, as well as the biomechanical considerations needed for drilling, polycarbonate was chosen as the best material for use in a scaphoid model.

### 4.4 Model Creation

Through additive manufacturing, a tunable scaphoid model made of polycarbonate was created in this study. By analyzing the bone density of scaphoids obtained from cadaver segments from the proximal to the distal end, the model was printed with five distinct regions of density. Additionally, the cortical shell of the scaphoid was also applied and able to be modified to fit the five different regions of density analyzed in this study. While the cadaver scaphoids and the models were specifically analyzed and made in this way for this study, they can be easily modified to print scaphoids of different sizes with different density values in other segmented areas, such as the anatomically segmented areas analyzed by Ahrend et al.[24]

Currently, no composite models have been validated for the biomechanical testing of the scaphoid. Additive manufacturing has been previously used for the in-house production of patient-specific scaphoid prostheses using medical-grade materials such as polyetheretherketone (PEEK).[46] Other models have used long-bone validated foam models to approximate the scaphoid structure and morphology.[25-27] The model in this study potentially bridges the gap of biomechanically relevant synthetic scaphoid models and can be applied to prosthesis design in the future.

## 4.5 Limitations

The sample size of seven scaphoids for the CT bone density measurements may be too small to adequately represent the population and reflect the variation in geometry and bone density. Furthermore, the average age for the cadaver specimens is higher than the average age of people who usually suffer from scaphoid fractures, who are usually athletic and young.

To extract strength values from the bone density CT scans of the cadaver scaphoids, the Carter-Hayes equation was used for an approximation of strength from bone density.[43] However, this equation was developed from the testing of human and bovine long bones and may or may not be representative of the structure and strength of small carpal bones like the scaphoid. To our knowledge, no other equation specifically exists for the characterization of bone strength from bone density scans of carpal bones. Further testing is required to validate this equation for use in carpal bones.

Printing with the resin material introduced many potential variables that could affect its performance in this study. Compared to the Ultimaker materials, an additional software component was required to achieve the gyroid structure. In contrast, the additive-manufactured materials had the gyroid structure easily applied during slicing the 3D-printed model. Furthermore, the required porous structure to mimic cancellous bone proved difficult to achieve with the stereolithographic technique, as the remaining resin at the structure's core was difficult to remove before the drying and curing process could occur. As the UV light was used on the

exterior of the model, there was no way to quantify if the interior of the model was fully cured

and that may have contributed to the performance of the resin specimens.

**Chapter 5: CONCLUSION AND IMPLICATIONS**

The present study achieved a framework for printing a tunable, anisotropic model of the scaphoid with fusion deposition modeling using a biomechanically tested polycarbonate material with gyroid structure. PLA, resin, and polycarbonate materials are all viable contenders for synthetically replicating the bone strength required. However, PLA may melt while drilling and the manufacturing process for SLA printing of resin was unreliable, making the polycarbonate material the best choice for this model. Furthermore, the difference in morphology seen within the cadaver scaphoids in this and other studies can be easily modeled and printed within this framework.

While the model was based on strength values extracted from measured cadaver bone densities, future studies need to be done to ensure that the biomechanical performance of the model is comparable to that seen in cadaver studies. A microstructural analysis should be done to look at the frictional forces of the different materials when inserting pins and screws. Other materials may prove to be better than the present material chosen for this study. As additive manufacturing methods are continuously improving, it is possible that new patterns and materials may prove to be better than polycarbonate if the manufacturing process can be refined and reproduced more uniformly. Establishing a scaphoid model opens the door to replicating all other carpal and metacarpal bones in the hand for use in biomechanical testing and evaluation of fracture fixation methods. This basic model can be augmented in the future with ligaments to apply physiological forces and further aid in the evaluation of surgical fixation methods.

**APPENDIX**

The scaphoids in this study were used in an additional study to test alternative K-wire configurations for treating scaphoid nonunion, a worst-case scenario. Scaphoids with simulated nonunion defects were used to compare the fixation with parallel and convergent configurations of K-wires. Specifically, the strength and stiffness of convergent and parallel K-wire configurations with a biomechanical, cadaveric model using a simulated non-union with a 3-mm defect were investigated. Interfragmentary motion, relative rotation between the proximal and distal fragments, and maximum force required to displace the scaphoid were measured.

Methods

Cadaver specimens were acquired through a licensed willed-body program after approval of the study protocol and faculty approval. Nine pairs of fresh-frozen cadaveric arms were used (n =18). After the scaphoids were dissected from each arm and freed from attached soft tissue, radiographs were taken of each bone to ensure there were no prior surgeries, fractures, or abnormalities.

*Creation of Fracture Model and Fixation*

Paired scaphoids were randomized to either a parallel or convergent pin orientation such that there were five left scaphoids assigned to the convergent group and four assigned to the parallel group. Accordingly, there were five right scaphoids in the parallel group and four in the convergent group.

Two custom targeting devices were created to reproducibly insert of K-wires into the bone in parallel and convergent orientations. In both configurations, scaphoids were mounted in the targeting device with 0.9mm (0.035") K-wires entering the volar aspect of the distal pole and engaging the midpoint of the proximal pole in the coronal plane. In the parallel configuration, K-wires were oriented such that they were aligned with the long axis of the scaphoid, maximizing the spacing between wires while ensuring that the wires were contained fully within the bone. In the convergent orientation, the wires were placed at a 15° angle to each other, meeting just beyond the proximal pole of the scaphoid.

Once mounted, the bone was secured with hot melt adhesive to maintain alignment throughout the process of creating the fracture model. The 0.9 mm K-wires were withdrawn into the distal pole, after which a fine coping saw was used to create a 5mm wedge osteotomy at the volar surface of the mid-waist of the bone, converging slightly proximal to the dorsal cortex. Following the creation of the defect, a 6 mm burr was used to remove cancellous bone from the proximal and distal poles to a depth of 6 mm. The 0.9 mm K-wires were then removed completely and replaced by 1.1 mm K-wires, pre-measured to the bone's exact length to ensure the cortical bone's engagement in the proximal fragment while preventing protrusion through the articular surface. Two 0.9 mm K-wires were also inserted into the distal fragment of the scaphoid as alignment guides for load testing. The first was inserted volar to dorsal, perpendicular to the transverse axis of the bone, and the second was placed lateral to medial at a 15° angle to the transverse axis of the distal pole. A 1.1mm K-wire was inserted into the proximal fragment of the scaphoid as a support for a 3D motion tracker flag. The fracture was completed through the dorsal cortex after the construct was mounted onto the load frame. After completion of fracture

model. After specimen preparation, the specimens were removed from the mold and placed into a potting apparatus for mechanical testing..
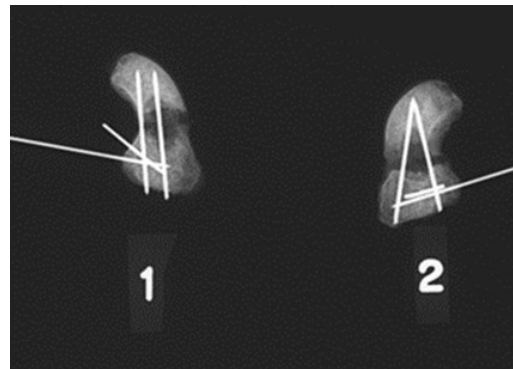


Figure 14: Parallel (1) and Convergent (2) Pin Configurations in cadaver scaphoids.

Biomechanical Testing

The distal pole of each specimen was rigidly potted in a custom apparatus and oriented to ensure that the alignment pins in each fracture fragment were orthogonal to the load actuator. The apparatus was subsequently mounted onto a biaxial MTS 858 MiniBionix servo-hydraulic load frame (MTS Systems, Minneapolis, MN). Using displacement control, a sinusoidal cyclic load was applied to the proximal end at 0.5mm/s to a peak displacement of 1 mm for 10 cycles. Then, a similar sinusoidal load was applied to a peak displacement of 2 mm for 10 cycles. Forces applied by the load frame and resultant displacements were continuously recorded during all each cycle.

 The interfragmentary motion was measured using an Optotrak 3020 Motion Capture System (Northern Digital Inc., Waterloo, Ontario, Canada). A motion tracker flag was attached to the

1.1mm support K-wire inserted into the proximal fragment of the scaphoid, while another was rigidly attached to the distal end potted onto the load frame.

## Data Reduction and Statistical Analysis

While the actuator applied an axial load to the proximal fragment, three-dimensional translations and rotations of the two fracture fragments in space were continuously recorded using the Optotrak system. Specifically, the fragments were free to translate in the horizontal plane or to rotate and deform under the applied axial load. Relative motions of the proximal and distal fragments of the scaphoid recorded by the Optotrak system and the load recorded by the MTS machine were interpolated with respect to time. The three-dimensional displacement of the proximal and distal fragments of the scaphoid was calculated by taking the square root of the sum of squares of the respective motions in the x, y, and z axes. The loads experienced by each specimen at different displacement values were plotted in a load vs. displacement curve. . The load and displacement values during the first cyclic loading test ( 1 mm peak actuator displacement ) was plotted to obtain the stiffness, calculated as the slope of the curve. Additionally, the maximum load was extracted at actuator displacement values of 0.5 and 1 mm. Finally, the maximum three-dimensional displacement (of fracture fragments) for each specimen was calculated using the minimum starting point, and the maximum displacement reached throughout testing.

## Stiffness Test

Eighteen scaphoids were prepared and fixed with K-wires, and axially compressed by the materials testing system. One scaphoid was omitted after it was found to be unstable and was

thus deemed unsuitable for testing in the load frame. The contralateral scaphoid was omitted as well due to a procedural error during testing. For the remaining 16 scaphoids, the axial compressive force was plotted against three-dimensional displacement through the scaphoid fracture site. (maximum displacement vector) data to obtain stiffness in the elastic region of Young's modulus curve for the fixation construction of scaphoid bones.  Stiffness values were then extracted and calculated from the linear region of force vs. displacement graphs for each specimen. The median stiffness for the convergent pin configuration was 81.6 N/mm whereas the parallel was 54.1 N/mm (p = 0.19).
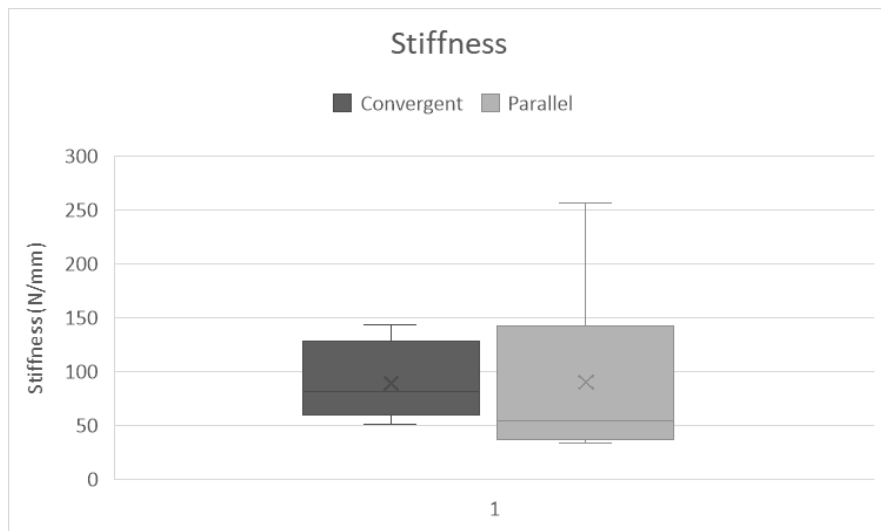


Figure 15: The X represents the average convergent and parallel stiffnesses. The Median line is represented by the horizontal line in the middle of each respective box. The 25th and 75th percentiles are represented by the edges of the box.

As shown in Figure 12, the average stiffness of the convergent and parallel pin configurations was comparable. However, the stiffness data was not normally distributed. The distribution for the parallel configuration is much wider and skewed to the right when compared to the more

symmetrical and narrowly distributed convergent pin configuration. Therefore, the analysis was based on a comparison of medians. The p-value was calculated using non-parametric tests, specifically the Mann-Whitney U-test.

*Maximum Force at 0.5 and 1 mm displacements*

A 0.5 mm actuator displacement was extracted for all the specimens from the 1 mm cantilever, as some specimens failed shortly after 0.5 mm displacement. The median maximum force for the convergent configuration was significantly higher than the parallel configuration, at a value of 36.5 N for convergent and 16.6 N for parallel (p = 0.04).
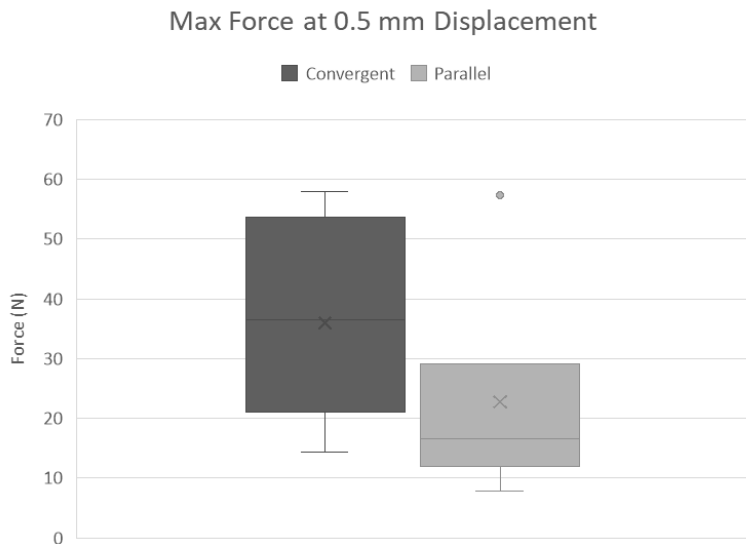


Figure 16: The X represents the average convergent and parallel maximum force at 0.5 mm displacement. The Median line is represented by the horizontal line in the middle of each respective box. The 25th and 75th percentiles are represented by the edges of the box.

The maximum force experienced under 1 mm of actuator displacement was $68.8 \pm 45.7$ N for the

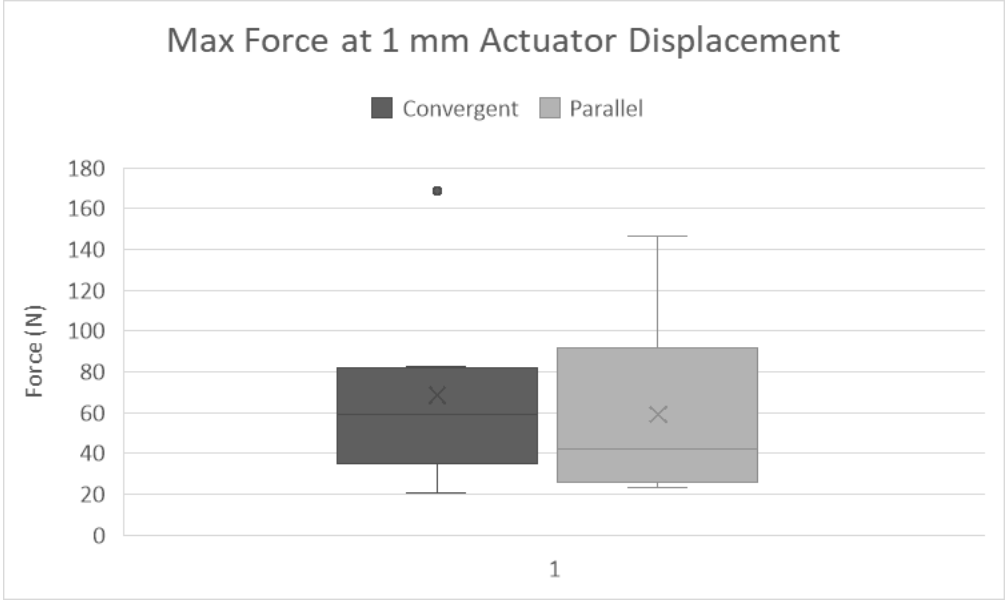convergent pin configuration and $59.0 \pm 43.9$ N for the parallel pin configuration (p = 0.67).



Figure 17: The X represents the average convergent and parallel maximum force at 1 mm displacement.
The Median line is represented by the horizontal line in the middle of each respective box. The 25th and
75th percentiles are represented by the edges of the box.

Discussion

Parallel and convergent K-Wire configurations have both been common methods of fracture

fixation in the scaphoid. However, the optimum configuration of K-wires is still unknown, and

few biomechanical studies have compared scaphoid fracture fixation configurations in a

cadaveric model. The present study is the first to use a cadaver model with simulated nonunion

under physiological loading to evaluate parallel versus convergent K-wires. Additionally, the

stiffness of the construct was calculated based on measurements of relative motion between the

fracture fragments using a six-degree-of-freedom optical motion tracking system. The results

suggested that convergent configurations were associated with significantly higher maximum force at 0.5 mm of actuator displacement and higher stiffness, as measured by the Optotrak system.

The present study was initially designed with the intention of using matched pairs for pairwise comparisons between parallel and convergent configurations. However, analysis of the data presented more consistent differences without pairing the data. Ceri et al. found significant differences between left and right pairs of scaphoids, suggesting that bone microarchitecture in dominant versus nondominant hands does change, perhaps based on Wolff's law.[21] Left and right differences were found in 4 morphometric features, including the waist circumference, which has the lowest east bone density compared to the proximal and distal portions of the scaphoid and is, therefore, the site of most of the scaphoid fractures. These left and right differences make it hard to utilize pairs of specimens as controls for each other. Therefore, we used comparisons between fixation groups in this study, regardless of laterality.

The median stiffness for the convergent pin configuration was larger than the parallel, with a narrower distribution. This suggests that the convergent configuration is more stable and consistent across a variety of different bones and situations, given the variation in morphology. The difference is also evident when evaluating the maximum force. The maximum force at an actuator displacement of 0.5 mm was significantly higher for the convergent configuration, indicating that the construct was more resistant to bending from the actuator force. From our

understanding of fracture stabilization, it would logically proceed that a convergent pin configuration should provide greater stability for mid-waist fractures, as the points of fixation achieve maximum spread across the fracture site, providing greater rotational stability to the construct. This may not apply to a proximal pole fracture for the same reason.

It is interesting that as the actuator displaced to 1 mm displacement, both the means and medians of both constructs increased and were relatively similar. There seems to be a threshold value past which pin configuration does not matter and both pins provide the same resultant force at a specific actuator displacement.

Final Remarks

This study simulated pin fixation for scaphoid nonunion, one of the worst scenarios after a scaphoid waist fracture. While the stability of K-wires compared to other fixation methods such as screws and plates has long been debated, this study was the first cadaveric study, to our knowledge, to test alternate K-wire configurations to characterize their stiffness and strength and be able to compare it to other fixation methods. It is the first biomechanical study to test fixation constructs by measuring fracture displacement rather than load to failure.

# REFERENCES

1. Charnley, J., & Kettlewell, J. (1965). The elimination of slip between prosthesis and femur. Journal of Bone and Joint Surgery. British Volume, 47-B(1), 56-60

2. Oh, I., & Harris, W. H. (1978). Proximal strain distribution in the loaded femur. Journal of Bone and Joint Surgery. American Volume, 60(1), 75-85

3. Markolf, K. L., & Amstutz, H. C. (1976). A comparative experimental study of stresses in femoral total hip replacement components: The effects of prosthesis orientation and acrylic fixation. Journal of Biomechanics, 9(4), 223-231

4. Crowninshield, R. D., Brand, R. A., Johnston, R. C., & Milroy, J. C. (1980). An analysis of femoral component stem design in total hip arthroplasty. Journal of Bone and Joint Surgery. American Volume, 62(1), 68-78

5. McKellop, H., Ebramzadeh, E., Fortune, J., & Sarmiento, A. (1989). Stability of subtrochanteric femoral fractures fixed with interlocking intramedullary rods. *ASTM Selected Technical Papers*, 1008, 202-218

6. McKellop, H., Ebramzadeh, E., Niederer, P. G., & Sarmiento, A. (1991). Comparison of the stability of press-fit hip prosthesis femoral stems using a synthetic model femur. *Journal of orthopaedic research : official publication of the Orthopaedic Research Society*, *9*(2), 297–305. https://doi.org/10.1002/jor.1100090219

7. Buford, W., Goswami, T., & Riggs, P. (2004). Evaluation of synthetic composite femur bones for use in hip prostheses studies: A photoelastic study. Journal of Biomechanics, 37(8), 1125-1133

8. Heiner, A. D., & Brown, T. D. (2001). Structural properties of a new design of composite replicate femurs and tibias. Journal of Biomechanics, 34(6), 773-781

9. Cristofolini, L., Viceconti, M., Cappello, A., & Toni, A. (1996). Mechanical validation of whole bone composite femur models. *Journal of biomechanics*, *29*(4), 525–535. https://doi.org/10.1016/0021-9290(95)00084-4

10. Cristofolini, L., Erani, P., Savigni, P., Grupp, T., Thies, O., & Viceconti, M. (2007). Increased long-term failure risk associated with excessively thin cement mantle in cemented hip arthroplasty: a comparative in vitro study. *Clinical biomechanics (Bristol, Avon)*, *22*(4), 410–421. https://doi.org/10.1016/j.clinbiomech.2006.09.001

11. Waide, V., Cristofolini, L., Stolk, J., Verdonschot, N., & Toni, A. (2003). Experimental investigation of bone remodelling using composite femurs. Clinical Biomechanics, 18(6), 523-536. https://doi.org/10.1016/S0268-0033(03)00072-X

12. Cristofolini, L., Affatato, S., Erani, P., Leardini, W., Tigani, D., & Viceconti, M. (2008). Long-term implant-bone fixation of the femoral component in total knee replacement. *Proceedings of the Institution of Mechanical Engineers. Part H, Journal of engineering in medicine*, *222*(3), 319–331. https://doi.org/10.1243/09544119JEIM328

13. Sangiorgio, S. N., Longjohn, D. B., Lee, J. L., Alexander, J. D., Dorr, L. D., & Ebramzadeh, E. (2008). Simulation of extreme loads on the proximal femur for implant fixation assessment. *Journal of applied biomaterials & biomechanics : JABB*, *6*(2), 72–80.

14. Sangiorgio, S. N., Ebramzadeh, E., Longjohn, D. B., & Dorr, L. D. (2004). Effects of dorsal flanges on fixation of a cemented total hip replacement femoral stem. *The Journal of bone and joint surgery. American volume*, *86*(4), 813–820. https://doi.org/10.2106/00004623-200404000-00022

15. Reed, J. D., Stanbury, S. J., Menorca, R. M., & Elfar, J. C. (2013). The emerging utility of composite bone models in biomechanical studies of the hand and upper extremity. The Journal of hand surgery, 38(3), 583–587. https://doi.org/10.1016/j.jhsa.2012.12.005

16. Metzner, F., Neupetsch, C., Carabello, A., Pietsch, M., Wendler, T., & Drossel, W. G. (2022). Biomechanical validation of additively manufactured artificial femoral bones. BMC biomedical engineering, 4(1), 6. https://doi.org/10.1186/s42490-022-00063-1

17. Haisman, J. M., Rohde, R. S., Weiland, A. J., & American Academy of Orthopaedic Surgeons (2006). Acute fractures of the scaphoid. The Journal of bone and joint surgery. American volume, 88(12), 2750–2758. https://doi.org/10.2106/00004623-200612000-00026

18. Brekke, A. C., Snoddy, M. C., Lee, D. H., Richard, M. J., & Desai, M. J. (2018). Biomechanical Strength of Scaphoid Partial Unions. Journal of wrist surgery, 7(5), 399–403. https://doi.org/10.1055/s-0038-1661362

19. Mandaleson, A., Tham, S. K., Lewis, C., Ackland, D. C., & Ek, E. T. (2018). Scaphoid Fracture Fixation in a Nonunion Model: A Biomechanical Study Comparing 3 Types of

Fixation. *The Journal of hand surgery*, *43*(3), 221–228.
https://doi.org/10.1016/j.jhsa.2017.10.005

20. Morimoto, M., Utsumi, M., Tohno, Y. et al. Age-related changes of bone mineral density in human calcaneus, talus, and scaphoid bone. Biol Trace Elem Res 82, 53–60 (2001). https://doi.org/10.1385/BTER:82:1-3:053

21. Ceri, N., Korman, E., Gunal, I., & Tetik, S. (2004). The morphological and morphometric features of the scaphoid. *Journal of hand surgery (Edinburgh, Scotland)*, *29*(4), 393–398. https://doi.org/10.1016/j.jhsb.2004.02.006

22. Letta, C., Schweizer, A., & Fürnstahl, P. (2014). Quantification of contralateral differences of the scaphoid: a comparison of bone geometry in three dimensions. Anatomy research international, 2014, 904275. https://doi.org/10.1155/2014/904275

23. Patterson, R. M., Elder, K. W., Viegas, S. F., & Buford, W. L. (1995). Carpal bone anatomy measured by computer analysis of three-dimensional reconstructions of computed tomography images. *The Journal of hand surgery*, *20*(6), 923–929. https://doi.org/10.1016/S0363-5023(05)80138-8

24. Ahrend, M. D., Teunis, T., Noser, H., Schmidutz, F., Richards, G., Gueorguiev, B., & Kamer, L. (2021). 3D computational anatomy of the scaphoid and its waist for use in fracture treatment. Journal of orthopaedic surgery and research, 16(1), 216. https://doi.org/10.1186/s13018-021-02330-8

25. Swanstrom, M. M., Morse, K. W., Lipman, J. D., Hearns, K. A., & Carlson, M. G. (2018). Variable Bone Density of Scaphoid: Importance of Subchondral Screw Placement. Journal of wrist surgery, 7(1), 66–70. https://doi.org/10.1055/s-0037-1605381

26. Gokce V, Oflaz H, Dulgeroglu A, Bora A, Gunal I. Kirschner wire fixation for scaphoid fractures: an experimental study in synthetic bones. J Hand Surg Eur Vol. 2011 May;36(4):325-8. doi: 10.1177/1753193410394525. Epub 2011 Jan 31. PMID: 21282225.

27. Erhart, J., Unger, E., Trulson, I., Hagmann, M., Ristl, R., Trulson, A., Hajdu, S., Schefzig, P., Gormasz, A., & Mayr, W. (2020). Pull-out forces of headless compression screws in variations of synthetic bone models imitating different types of scaphoid fractures in good bone quality. *Journal of materials science. Materials in medicine*, *31*(11), 92. https://doi.org/10.1007/s10856-020-06445-y

28. Lebowitz, C., Massaglia, J., Hoffman, C., Lucenti, L., Dheer, S., Rivlin, M., & Beredjiklian, P. K. (2021). The Accuracy of 3D Printed Carpal Bones Generated from Cadaveric Specimens. The archives of bone and joint surgery, 9(4), 432–438. https://doi.org/10.22038/abjs.2020.50236.2495

29. Emer, M. Ö., İnce, S., & Arslan, N. (2016). Bone mineral densitometry: Measurement and evaluation methods. In F. Korkusuz (Ed.), Musculoskeletal research and basic science (pp. 169-188). Springer. https://doi.org/10.1007/978-3-319-20777-3_12

30. Turner, I. G., & Rice, G. N. (1992). Comparison of bone screw holding strength in healthy bovine and osteoporotic human cancellous bone. *Clinical materials*, *9*(2), 105–107. https://doi.org/10.1016/0267-6605(92)90054-w

31. Alho A. (1993). Mineral and mechanics of bone fragility fractures. A review of fixation methods. *Acta orthopaedica Scandinavica*, *64*(2), 227–232. https://doi.org/10.3109/17453679308994578

32. Alonso-Vázquez, A., Lauge-Pedersen, H., Lidgren, L., & Taylor, M. (2004). The effect of bone quality on the stability of ankle arthrodesis. A finite element study. *Foot & ankle international*, *25*(11), 840–850. https://doi.org/10.1177/107110070402501115

33. Yeni, Y. N., Brown, C. U., Wang, Z., & Norman, T. L. (1997). The influence of bone morphology on fracture toughness of the human femur and tibia. *Bone*, *21*(5), 453–459. https://doi.org/10.1016/s8756-3282(97)00173-7

34. Melton, L. J., Beck, T. J., Amin, S., & others. (2005). Contributions of bone density and structure to fracture risk assessment in men and women. *Osteoporosis International, 16*(5), 460–467. https://doi.org/10.1007/s00198-004-1820-1

35. Muriuki, M. G., Reddy, A. K., Tauchen, A., Havey, R. M., Patwardhan, A. G., & Bindra, R. R. (2023). Effect of K-wire Reuse and Drill Mode on Heat Generation in Bone. Hand (New York, N.Y.), 18(2), 314–319. https://doi.org/10.1177/15589447211003172

36. van Egmond, D. B., Hovius, S. E., van der Meulen, J. C., & den Ouden, A. (1994). Heat recordings at tips of Kirschner wires during drilling through human phalanges. The Journal of hand surgery, 19(4), 648–652. https://doi.org/10.1016/0363-5023(94)90275-5

37. Nägl, K., Reisinger, A., & Pahr, D. H. (2022). The biomechanical behavior of 3D printed human femoral bones based on generic and patient-specific geometries. *3D printing in medicine*, *8*(1), 35. https://doi.org/10.1186/s41205-022-00162-8

38. Favier, V., Zemiti, N., Caravaca Mora, O., Subsol, G., Captier, G., Lebrun, R., Crampette, L., Mondain, M., & Gilles, B. (2017). Geometric and mechanical evaluation of 3D-printing materials for skull base anatomical education and endoscopic surgery simulation - A first step to create reliable customized simulators. PloS one, 12(12), e0189486. https://doi.org/10.1371/journal.pone.0189486

39. McMillan, A., Kocharyan, A., Dekker, S. E., Kikano, E. G., Garg, A., Huang, V. W., Moon, N., Cooke, M., & Mowry, S. E. (2020). Comparison of Materials Used for 3D-Printing Temporal Bone Models to Simulate Surgical Dissection. The Annals of otology, rhinology, and laryngology, 129(12), 1168–1173. https://doi.org/10.1177/0003489420918273

40. Wahbeh, J. M., Hookasian, E., Lama, J., Alam, L., Park, S. H., Sangiorgio, S. N., & Ebramzadeh, E. (2023). An additively manufactured model for preclinical testing of cervical devices. *JOR spine*, *7*(1), e1285. https://doi.org/10.1002/jsp2.1285

41. Silva, C., Pais, A. I., Caldas, G., Gouveia, B. P. P. A., Alves, J. L., & Belinha, J. (2021, May 31). Study on 3D printing of gyroid-based structures for superior structural behaviour - progress in additive manufacturing. SpringerLink. https://link.springer.com/article/10.1007/s40964-021-00191-5

42. Mandaleson A, Tham SK, Lewis C, Ackland DC, Ek ET. Scaphoid Fracture Fixation in a Nonunion Model: A Biomechanical Study Comparing 3 Types of Fixation. J Hand Surg Am. 2018 Mar;43(3):221-228. doi: 10.1016/j.jhsa.2017.10.005. Epub 2017 Nov 11. PMID: 29132789

43. Carter, D. R., & Hayes, W. C. (1977). The compressive behavior of bone as a two-phase porous structure. *The Journal of Bone & Joint Surgery*, 59(7), 954-962.

44. Bohl, M. A., Morgan, C. D., Mooney, M. A., Repp, G. J., Lehrman, J. N., Kelly, B. P., Chang, S. W., Turner, J. D., & Kakarla, U. K. (2019). Biomechanical Testing of a 3D-printed L5 Vertebral Body Model. Cureus, 11(1), e3893. https://doi.org/10.7759/cureus.3893

45. Honigmann, P., Sharma, N., Schumacher, R., Rueegg, J., Haefeli, M., & Thieringer, F. (2021). In-Hospital 3D Printed Scaphoid Prosthesis Using Medical-Grade

Polyetheretherketone (PEEK) Biomaterial. BioMed research international, 2021, 1301028. https://doi.org/10.1155/2021/1301028

46. ASTM International. (2015). Standard test method for compressive properties of rigid plastics (ASTM Standard D695-15). ASTM International. https://doi.org/10.1520/D0695-15

47. Galvez, M., Asahi, T., Baar, A., Carcuro, G., Cuchacovich, N., Fuentes, J. A., Mardones, R., Montoya, C. E., Negrin, R., Otayza, F., Rojas, G. M., & Chahin, A. (2018). Use of Three-dimensional Printing in Orthopaedic Surgical Planning. Journal of the American Academy of Orthopaedic Surgeons. Global research & reviews, 2(5), e071. https://doi.org/10.5435/JAAOSGlobal-D-17-00071

48. Huntington, L. S., Mandaleson, A., Hik, F., Ek, E. T. H., Ackland, D. C., & Tham, S. K. Y. (2020). Measurement of Scaphoid Bone Microarchitecture: A Computed Tomography Imaging Study and Implications for Screw Placement. The Journal of hand surgery, 45(12), 1185.e1–1185.e8. https://doi.org/10.1016/j.jhsa.2020.05.028